Proceedings of Global Power and Propulsion Society
ISSN-Nr: 2504-4400
GPPS Hong Kong23
17 – 19 October, 2023
www.gpps.global

GPPS-TC-2023-0027

UNSTEADY FLOW PHENOMENON IN THE TUDA-GLR-OPENSTAGE COMPRESSOR: URANS OBSERVATIONS

Hefang Deng[1], **Xiao He**[2,*], **Mingmin Zhu**[1], **Fabian Klausmann**[3], **Jinfang Teng**[1]
[1] School of Aeronautics and Astronautics, Shanghai Jiao Tong University, Shanghai 200240, China
[2] Department of Aeronautics, Imperial College London, London SW7 2AZ, UK
[3] Institute of Gas Turbines and Aerospace Propulsion, Technische Universität Darmstadt, Darmstadt 64287, Germany
*Correspondence: xiao.he2014@imperial.ac.uk

ABSTRACT

Unsteady flow phenomenon plays a critical role in determining the aerodynamic performance and stability of a compressor. In this study, the unsteady flow phenomena in the TUDa-GLR-OpenStage compressor at stable operating conditions were investigated through unsteady Reynolds-Averaged Navier-Stokes (URANS) simulations. The URANS results were first validated against measured data in terms of mean flow quantities and unsteady fluctuations. Then, the unsteady flow phenomena and their associated flow mechanisms in the rotor tip region, the stator hub region, and the stator hub cavity were discussed in detail. The results show that at the rotor tip, URANS captures the fluctuations associated with the blade passing frequency (BPF) and its harmonics, but it fails to capture sub-BPF fluctuations of tip leakage flow observed in the measured data. At the stator hub, URANS captures the rotor-stator interaction at the BPF, and the unsteady fluctuation of stator hub corner separation with the rotor wake phase is analyzed. At the stator hub cavity, URANS captures a broadband low-frequency signal in the cavity exit channel, which corresponds to the pumping mode of the blockage cells that leads to the unsteady fluctuation of leakage flow rate. These results provide valuable information on the unsteady flow mechanisms of the investigated compressor and the capability of URANS simulations for predicting compressor flows at stable operating conditions.

1 INTRODUCTION

The internal flows of axial compressors, such as tip leakage flow, corner separation, and shock-boundary layer interaction, exhibit inherent unsteadiness. With the growing need for cleaner aviation, the design objectives for the next-generation axial compressor involve higher aerodynamic loading, which further stimulates unsteady flow phenomena in compressors. Hence, an enhanced understanding of unsteady flows is crucial for the design of next-generation compression systems.

To simulate unsteady flow phenomena in axial compressors, the most accurate methods are scale-resolving simulations such as large eddy simulation and direct numerical simulation, which can resolve most scales of unsteady fluctuations. However, their computational costs increase substantially with the Reynolds number of the problem, which limits their applicability to industrial flows. Alternatively, URANS can capture both large-scale unsteadiness (e.g., surge and stall) and deterministic unsteadiness (e.g., rotor-stator interaction) well. When a refined grid and a small time step are used, URANS can also partially resolve the unsteadiness of the sub-passage scale. This approach achieves a balance between accuracy and computational cost, making it the most commonly used unsteady simulation method for axial compressors. Nevertheless, validation of URANS simulations was often limited to mean flow quantities, making it difficult to assess their capability to predict unsteady compressor flows in the sub-passage scale. There is only a few previous research comparing URANS results with high-fidelity numerical or experimental results [1–4]. The general findings are that URANS tends to underestimate the pressure and velocity fluctuations [1, 4], and the predicted frequency of the sub-passage unsteady flow phenomenon can be right in one case [3] but wrong in another [2, 4]. Therefore, further evaluation of URANS in more compressor cases is still needed.

For the physical understanding of the unsteady compressor flow phenomenon, previous research has made significant strides in a range of unsteady compressor flow phenomena through the use of unsteady simulations and transient measurements.

Regarding the rotor tip leakage flow, Mailach et al. [5] performed experimental measurements on a low-speed axial compressor with a large tip clearance. It was found that the unsteady fluctuation of tip leakage flow and its interaction with the flow of the adjacent blade can lead to a broadband rotating disturbance signal (also known as rotating instability), whose average circumferential count is about half of the rotor blade number. In a different study by Marz et al. [6], it was again concluded that the formation and the traveling (with the wave speed about half of the rotor speed) of the tip leakage vortex are responsible for the rotating disturbance. By performing full-annulus URANS simulations, Wang et al. [3] observed that when the tip leakage vortex propagates to the adjacent blade, it interacts with the pressure surface of the adjacent blade and starts to oscillate, resulting in a short-length rotating disturbance. Du et al. [7] found single-frequency self-induced unsteadiness in a transonic rotor by conducting URANS simulations. The study revealed that this phenomenon occurs when the tip leakage flow is strong enough to impinge on the pressure side of the neighboring blade. Zhu et al. [8] analyzed the unsteady near-stall flow mechanisms of a transonic compressor rotor at various rotational speeds. The results indicated that the shock front and consequently the shock-induced tip leakage vortex breakdown is located further upstream when the rotational speed reduces.

Regarding the rotor-stator blade row interaction, Mailach et al. [9] conducted transient measurements that unveiled the interaction between the upstream stator wake and the downstream rotor tip clearance vortex. The results identified periodic changes in the circumferential extension and the flow orientation of the tip leakage vortex synchronized with the incoming wake. Montomoli et al. [10] found in a multistage cantilevered compressor that the near-hub efficiency of the URANS simulation is higher than that of the RANS simulation. This is attributed to the periodical interaction of the rotor wake and stator hub leakage flow. Specifically, the rotor wake is reoriented by the hub leakage vortex in the stator passage, resulting in a direction that is more parallel to the main flow. Additionally, the periodic passing of the rotor intercepts a portion of the double leakage flow. These factors observed from the URANS simulation tend to reduce the loss near the hub. Saito et al. [11] found that the wake of the upstream rotor exerts a more substantial influence on the stator flow compared to the shock wave of the downstream rotor. In particular, the rotor wake induces periodic variations in the foci-type separation on the stator suction surface.

Regarding the stator corner separation, the pioneering work of Schulz et al. [12] experimentally investigated the unsteady effect of the upstream wake on the corner separation of an annular compressor cascade. They found that the unsteady upstream wake can reduce the corner separation size, especially at smaller incidence conditions. Ma et al. [13] reported for the first time a bimodal phenomenon (characterized by bimodal histograms of measured velocity) in intermittent corner separation. Their results revealed that this bimodal phenomenon primarily occurs near the interface between attached and separated flows. Liu et al. [14] found unsteady fluctuation of corner separation via DDES simulations, and the evolution of vortical structures was also described. More recently, Dawkins et al. [15] conducted experimental investigations on the unsteady flow topology of corner separation. In contrast to the time-averaged flow field, the time-resolved flow field exhibits numerous focus and saddle pairs produced stochastically at the blade corner, and a large-scale unsteady motion of the corner separation was captured.

Regarding the stator cavity leakage flow, Wellborn [16] first investigated the details of shrouded stator cavity flows via URANS, and deterministic unsteadiness from the upstream rotor wake was observed in the cavity channel. Lee et al. [17] conducted measurements of the periodic unsteady flow field of a shrouded stator. Their findings revealed that the combination of cavity leakage flow and the upstream rotor wake leads to periodic variations in the radial gradients of axial and tangential velocities, resulting in the generation of unsteady streamwise vorticity.

Based on the literature review above, it is evident that a broad range of unsteady flow phenomena exists in each component of an axial compressor, which affects the performance of the compressor. Among these flow phenomena, the unsteady flow phenomena in the stator cavity, in particular, are not well understood due to the limited number of case studies reported in the literature. Therefore, unsteady simulations and measurements for stator cavity flow are of high interest.

This paper conducts a numerical case study using URANS on the TUDa-GLR-OpenStage compressor, and the main objectives are twofold: (1) evaluate the extent to which URANS can capture unsteady flow phenomena in an axial compressor; (2) conduct an initial URANS investigation of the unsteady flow phenomena in the rotor tip region, the stator hub region, and the stator hub cavity of the TUDa-GLR-OpenStage. The remainder of the paper is organized as follows. First, the compressor and numerical setup used in this work will be introduced. Then, the mean flow quantities will be validated and analyzed, including the overall performance characteristics and the detailed flow field. Afterward, the unsteady flow phenomena in the rotor tip region, stator hub region, and stator hub cavity will be analyzed respectively.

2 METHODOLOGY

2.1 Case Description

The investigated TUDa-GLR-OpenStage compressor [18] represents a front stage of a commercial engine. It comprises 16 CDA-airfoil rotor blades, 29 shrouded stator blades, and 5 outlet guide vane (OGV) blades, as well as a rotating nose cone and a stator hub seal cavity. This compressor is known to exhibit abundant unsteady flow phenomena, such as shock-tip leakage flow interaction, rotor-stator interaction, and corner separation [19]. Therefore, it is an ideal benchmark case for investigating unsteady flow phenomena in axial compressors.

Extensive measurement data for the TUDa-GLR-OpenStage compressor have been made available by GLR in past GPPS events. Specifically, the first dataset was released in the year 2020 [18], which includes the boundary layer rakes data at the inlet (ME15 section), the five-hole probe data at the rotor exit (ME21 section), and the combined Kielhead probes data at the stage exit (ME30 section). This dataset was used in the first GPPS RANS CFD workshop, and an evident difference between all CFD submissions and the measured data was observed at the stage exit near the hub. Following the workshop, a repeat measurement was performed, with only minor differences observed compared to the first dataset. The data of the repeat measurement along with the Kulite probes data on the rotor casing [19] were released in the year 2022. The sampling frequency of the Kulite probes is about 93.75 BPF (i.e., 500 kHz), which is sufficiently large to capture the major unsteady flow features in the compressor. More recently, GLR has performed an additional measurement on a case with an increased stator cavity seal clearance [20]. This geometry is numerically investigated in this work, and the corresponding measured performance characteristics will be compared with the simulation data. In addition, it is assumed that the change in stator cavity geometry will mainly change the flow field of the stator but not the rotor. Therefore, the rotor casing Kulite data, the rotor exit profiles, and the stage exit total temperature profiles (determined by the rotor work input) obtained from the previous geometry with smaller cavity leakage can be used for validation. The stage exit total pressure profiles of the previous geometry, on the other hand, over-estimates the near-hub total pressure of the current geometry. This data will be used for qualitative comparison for completeness.

The measurements have been carried out at various rotational speeds and mass flow rates, and this paper focuses on the peak efficiency (PE) and near stall (NS) conditions at 100% (transonic) and 65% (subsonic) design speeds, respectively. It is worth noting that the operating conditions were named based on the URANS simulation results, whose mass flow rate is 15.83 kg/s for PE condition of 100% speed, 14.19 kg/s for NS condition of 100% speed, 10.41 kg/s for PE condition of 65% speed, and 8.47 kg/s for NS condition of 65% speed.

2.2 Flow Solver

All simulations in this study were conducted using Ansys CFX (version 2020R1), a widely used commercial 3D RANS flow solver for turbomachinery research. The RANS equations in Ansys CFX were discretized by an element-based finite volume method using unstructured meshes. The discrete system of linearized equations was solved using the incomplete lower-upper factorization technique and was simultaneously accelerated by an algebraic multigrid method. To determine turbulent viscosity, the Baseline Explicit Algebraic Reynolds Stress Model (BSL EARSM) [21, 22] was employed with automatic wall functions and fully turbulent boundary layers. The BSL EARSM model is theoretically advantageous in predicting system rotation, secondary flows, and streamline curvature. For unsteady simulations, a dual-time-stepping algorithm was utilized. The backward Euler scheme and the upwind-biased high-resolution scheme were used as the temporal discretization scheme and spatial convective scheme, respectively, both of which were second-order accurate.

2.3 Computational Domain, Boundary Conditions and Grid Topology

Figure 1 shows the computational domain and boundary conditions for the TUDa-GLR-OpenStage compressor. The numerical model considers most of the detailed features of the test rig geometry, such as the stator hub seal cavity, the blade fillets of both rotor and stator, the rotor casing pinch, and the rotor hub nose cone. For steady RANS simulations, the domain comprises one rotor passage, one stator passage (with hub cavity), and one OGV passage. A pair of periodic boundary conditions are used on the side walls. The interfaces between the rotor and stator and between the stator and the OGV are modeled as mixing planes. The interface between the rotor and the stator hub cavity is modeled by a frozen-rotor boundary condition. For URANS simulations, the stator blade count is increased from 29 to 32, resulting in a periodic unit of one rotor passage and two stator passages. Such a flow domain is capable of capturing the unsteady phenomenon of sub-passage scales, which is sufficient for the purpose of this study. The interfaces between the rotor and the stator and between the rotor and the stator hub cavity are modeled as sliding planes. However, the interface between the stator and the OGV remains as a mixing plane since the unsteady phenomenon in the OGV is irrelevant in this study.

The inlet of the computational domain corresponds to the ME15 section of the measurement, and the measured 1D radial profiles of total pressure and total temperature are utilized to impose the inlet boundary conditions. The inlet turbulence intensity and turbulence length scale are set uniformly as 4% and 0.09 mm, respectively. At the exit, a converging nozzle is used to control the mass flow rate, and the static pressure is set to a low value of 50 kPa to choke the nozzle. By changing the nozzle throat area, the compressor operating condition can be adjusted.

The computational domain is discretized using high-quality hexahedral grids generated by Numeca AutoGrid5. The grid topology and grid density are similar to the Medium grid of the previous validation work, which shows a discretization error of about 1.3% in predicting the total pressure ratio [23]. To cope with the stator hub cavity, fully matching grids were used at the interfaces between the blade passages and the cavity to eliminate interpolation errors. Between the OGV and the converging nozzle, a buffer zone with a large grid stretching ratio was adopted to dampen out the acoustic reflections from the choked nozzle. The computational domain contains 4.3 million cells for steady simulations and 5.0 million cells for unsteady simulations, with approximately 1.0 million cells per rotor passage, 0.7 million cells per stator passage, 0.9 million cells per OGV passage, and 1.3 million cells per cavity passage.

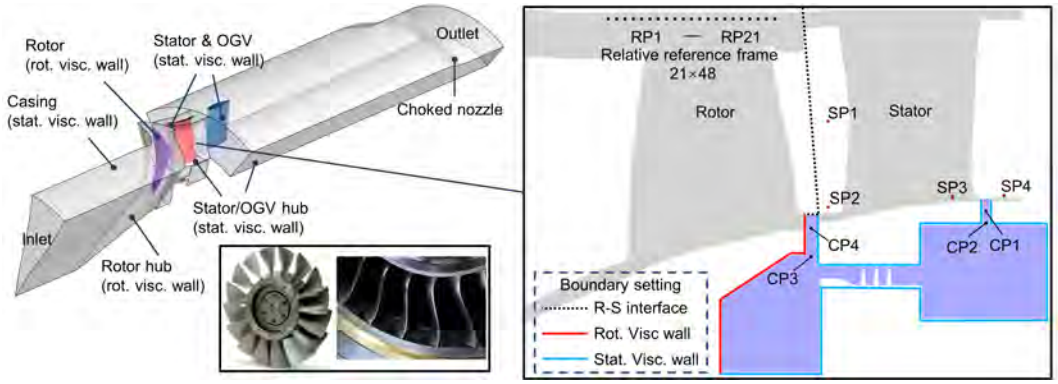

Figure 1: Illustration of the computational domain, boundary conditions, and locations of numerical probes.

For unsteady simulations, the physical time step is set to 3.91×10^{-6} s at 100% speed and 6.01×10^{-6} s at 65% speed, corresponding to 1/48 of the rotor blade passing time. The inner iteration for each physical time step is set to 5, which ensures the residual of the energy equation drops by two orders of magnitude. The URANS simulations have been performed for at least 5200 iterations (i.e., around 6.8 rotor revolutions) to achieve a statistically converged solution. Then, a further 960 iterations (i.e., around 20 blade passing periods) were performed to calculate the mean flow quantities and the standard deviations.

2.4 Numerical Probes

To help analyze the spectral property of the unsteady fluctuations, several numerical probes are monitored in the flow domain as indicated in Figure 1. For brevity, the numerical probes in the rotor domain, the stator domain and the cavity domain are referred to as RP, SP and CP, respectively. At the rotor casing, probes are distributed at 21 axial locations covering the entire rotor tip chord. At each axial position, 48 numerical probes are uniformly distributed along the circumferential direction, which allows the conversion of unsteady pressure from the relative frame to the absolute frame. The converted probes are referred to as RP1 to RP21. In the stator domain, 4 probes are monitored at the mid-pitch, with SP1 located at the mid-span upstream of the stator, and SP2, SP3 and SP4 located near the hub at different streamwise locations. In the cavity domain, 4 probes are monitored with CP1 and CP2 located at the center of the cavity outlet channel, and CP3 and CP4 located at the center of the cavity inlet channel.

3 ANALYSIS OF MEAN FLOW

3.1 Overall Performance Characteristics

Figure 2 illustrates the stage performance characteristics of simulations and experiments at 100% and 65% of the design speed. In these plots, the cases indicated by "29S" and "32S" represent simulated geometries with 29 and 32 stator blades, respectively. The total pressure ratio π_{15-30} is defined using the area-averaged total pressure, and the isentropic efficiency η_{15-30} is defined using the mass-averaged total temperature and the area-averaged total pressure. These definitions are physically consistent with that used in the experiment [18].

Overall, the trends of the total pressure ratio and adiabatic efficiency characteristics curves are well captured by both steady RANS simulations, despite minor deficiencies with regard to the NS total pressure ratio. However, such deficiencies can be alleviated when URANS simulation is adopted, as the time-averaged URANS predictions on the NS total pressure ratio match reasonably well with the measured data. Comparing both RANS results with different numbers of stator blades, no evident differences were observed, indicating the re-scaling of stator blade count barely changes the overall compressor performance.

Figure 3 presents the axial distribution of the circumferentially-averaged normalized static pressure $p/p_{t,15}$ on the rotor casing. Here, the axial location in the horizontal axis is non-dimensionalized by the rotor tip axial chord, with coordinates 0 and 1 denoting the LE and the TE of the rotor blade, respectively. Results show good agreement between the experimental data and the time-averaged URANS results. Besides, both experimental and URANS results show an increase in the pressure rise (i.e., Δp) and front blade loading (i.e., $\partial p/\partial x$) as the compressor operates toward stall, which is expected.

Figure 4 presents the circumferentially-averaged radial profiles of total pressure ratio π_{15-30} and total temperature ratio τ_{15-30} at the stage exit (ME30). At the PE condition of both speeds, the total pressure ratio and total temperature ratio of the experiment and simulations show good agreement with each other, indicating that URANS of the scaled geometry captures the mean flow physics at the PE condition correctly.

At the NS condition of 100% speed, the steady RANS result of the original stator blade count shows a similar trend to the measured data, but that of the increased stator blade count predicts an evidently smaller near-tip separation size and hence overpredicts the total pressure ratio near 80% span. Such a difference is caused by the scaling of the stator blade count, which can be alleviated by changing the chord length and the stagger angle of the stator blade to maintain the same throat area and solidity. In addition,

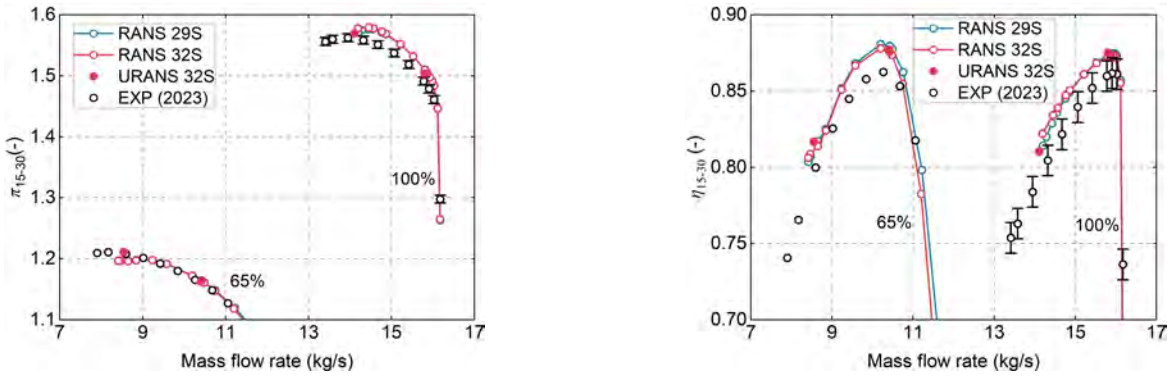

(a) Total pressure ratio.

(b) Adiabatic efficiency.

Figure 2: Comparison of stage performance characteristics between experimental and numerical results.

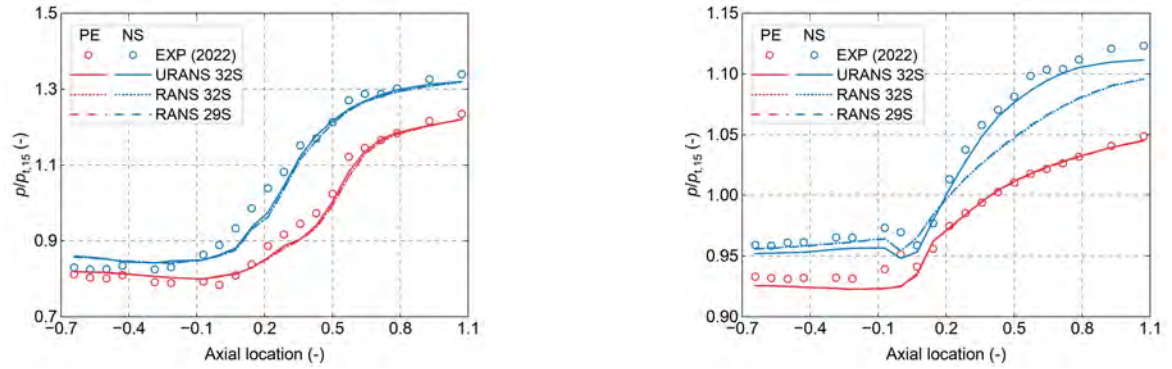

(a) 100% speed.

(b) 65% speed.

Figure 3: Comparison of time-averaged normalized static pressure at the rotor casing.

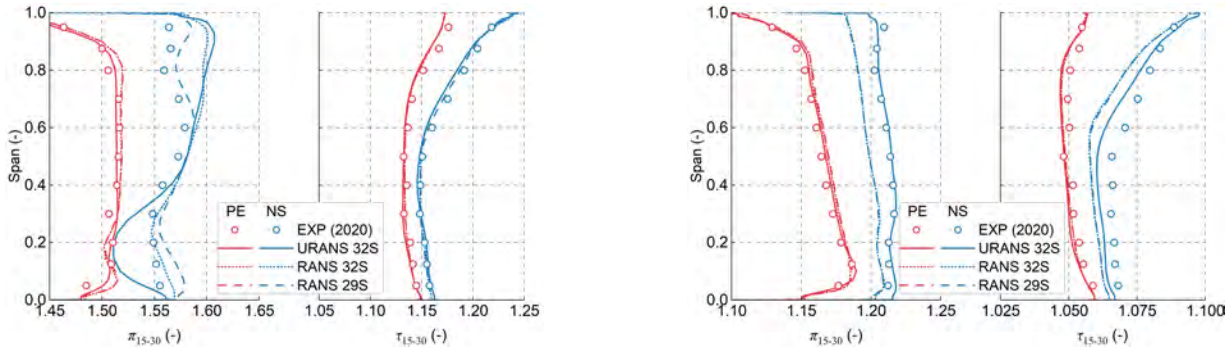

(a) 100% speed.

(b) 65% speed.

Figure 4: Comparison of radial profiles of stage exit (ME30) between experimental and numerical results.

URANS predicts an earlier corner stall than RANS does. Therefore, URANS of the scaled geometry can only capture the near-hub mean flow physics qualitatively at the NS condition of the 100% speed.

At the NS condition of 65% speed, both RANS simulations overlap with each other, indicating the effect of the blade count scaling is minimal. However, both results underpredict the total pressure ratio and total temperature ratio along the full span. On the other hand, URANS improves the prediction accuracy of the rotor deviation angle and thus the stage total temperature ratio and total pressure ratio.

3.2 Detailed Flow Field

To identify the major flow phenomena occurring within the rotor passage, Figure 5 presents the time-averaged normalized static pressure contours overlaid with the limiting streamlines on the rotor suction surface and the rotor hub surface. For all the operating

conditions, a single-sided hub corner separation is observed, which expands radially outward and axially upstream when throttling from the PE to the NS condition. This type of corner separation generally does not cause significant performance degradation [15]. At 100% speed, a part-span shock-induced separation dominates the flow field on the upper spans, expanding radially inward and axially upstream when throttling from the PE to the NS condition. At 65% speed, the flow field near the leading edge exhibits an approximately full-span leading-edge separation. The size of the leading-edge separation is small at the PE condition, but it significantly increases at the NS condition due to the high incidence. In the subsequent section of the unsteady analysis, the focus will be on the rotor near-tip flow phenomenon.

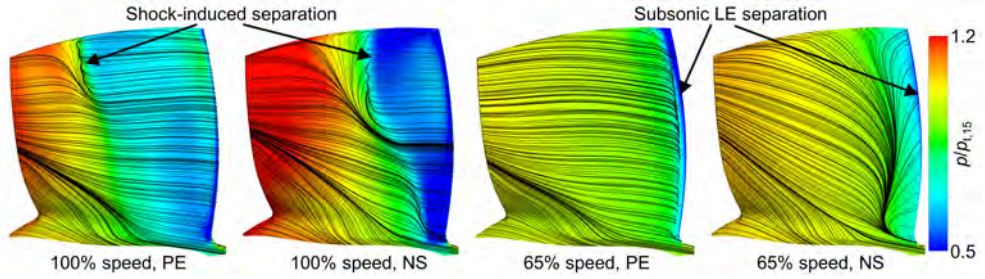

Figure 5: Time-averaged limiting streamline and normalized static pressure contours on the rotor suction surface and the rotor hub surface (flow coming from right to left).

To gain insights into the flow characteristics within the stator, Figure 6 presents the normalized static pressure contours overlaid with the surface limiting streamlines on the stator suction surface and the stator hub surface. In this figure, a hub corner separation is observed under all operating conditions, whose size is smaller at 65% speed than 100% speed and at the PE condition than the NS condition. This can be attributed to the reduced blade loading and hub cavity leakage flow rate. The formation of corner separation is generally influenced by the secondary flow and the pressure gradient in the streamwise and circumferential direction. In the subsequent section, it will be shown that the stator hub corner separation is also interactive with the unsteady rotor passing wake and the unsteady cavity leakage flow, both of which can be captured by URANS.

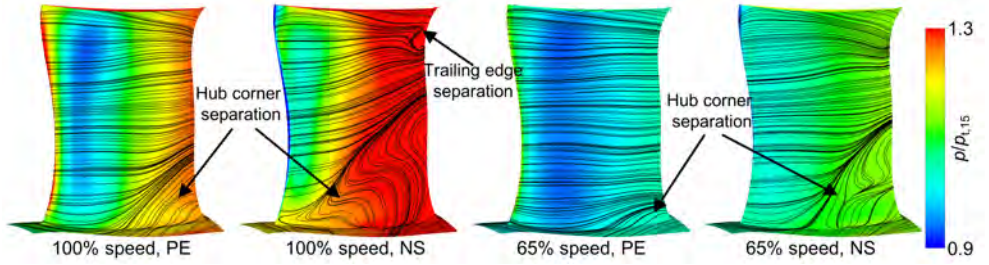

Figure 6: Time-averaged limiting streamline and normalized static pressure contours on the stator suction surface and the stator hub surface (flow coming from left to right).

Finally, to illustrate the mean flow physics of the stator hub cavity, Figure 7 depicts the time-averaged velocity magnitude contour at the cavity periodic boundary. Here, the velocity magnitude is normalized by the corresponding rotor blade speed at the midspan. In general, all operating conditions exhibit the same flow topology featured by a seal jet and an associated shear layer, indicating that the cavity flow physics is independent of the compressor operating conditions (results of the 100% speed, NS condition and the 65% speed, PE condition are not shown for brevity). The shear layer is formed at the interface between the high-speed seal jet of the seal gap and the low-speed wake of the seal tooth, where the local velocity gradient is large. The subsequent section will confirm that this flow structure is intrinsically unsteady and can be captured by URANS.

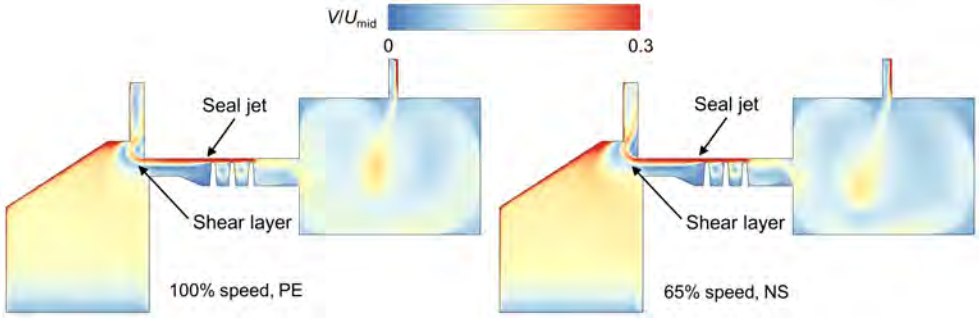

Figure 7: Time-averaged velocity magnitude contours at the cavity periodic boundary.

4 ANALYSIS OF UNSTEADY PHENOMENON IN ROTOR

This section analyzes the unsteady phenomena in the rotor with a focus on the near-tip region. Figure 8 compares the standard deviation of the static pressure at the rotor casing, where the standard deviation is normalized by the averaged total pressure at the rotor inlet ($p_{t,15}$). At 100% speed, URANS qualitatively predicts the trend of the standard deviation distribution. From the PE condition to the NS condition, the peak value of the standard deviation becomes larger, and its location moves further upstream. However, URANS consistently over-predicts the standard deviation at both conditions. At 65% speed, URANS accurately predicts the standard deviation at the NS condition, but it predicts a higher peak value and a further upstream peak location compared to the measured data.

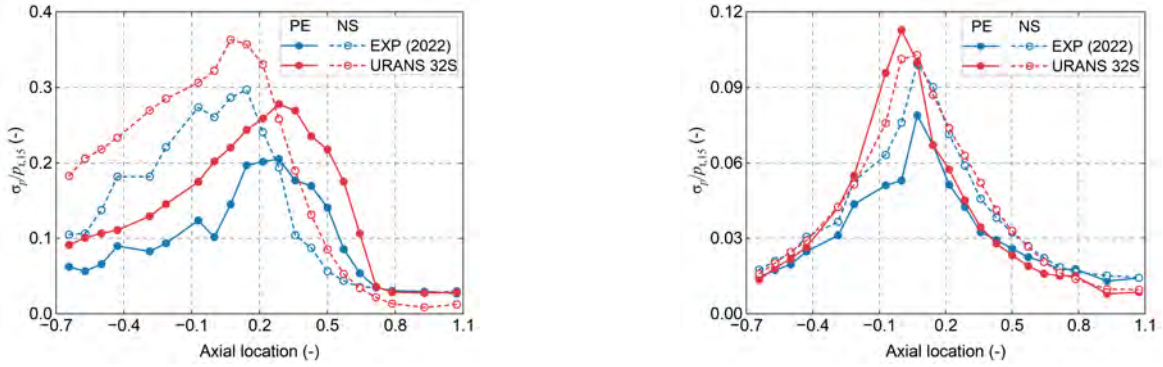

(a) 100% speed.

(b) 65% speed.

Figure 8: Comparison of the standard deviation of the normalized static pressure at the rotor casing.

To unveil the frequency component of the unsteady flow phenomenon captured by the experiment and the URANS simulations, power spectrum density (PSD) analysis of the rotor casing normalized wall pressure $p/p_{t,15}$ is performed. The PSD results of this work were calculated using the Welch method [24] with 50% overlap.

Figure 9 presents the PSD value as colored contours. In these plots, the horizontal axis denotes the axial location normalized by the rotor tip axial chord, with coordinates 0 and 1 representing the rotor LE and TE (also marked by the vertical dashed lines); the vertical axis represents the frequency normalized by the BPF. In general, the PSD results of the experiments and simulations showed significant differences. The experimental results present unsteady fluctuations with a broad range of frequencies, including frequency spikes at the BPF and its harmonics representing blade passing, and a frequency hump near 0.2 BPF (100%, NS condition) and near 0.8 BPF (65%, NS condition) reminiscent of rotating disturbance [5]. The URANS simulations, however, only capture the blade passing signals and a low-frequency signal at 0.1 BPF (65%, NS condition) that potentially represents a numerical rotating disturbance.

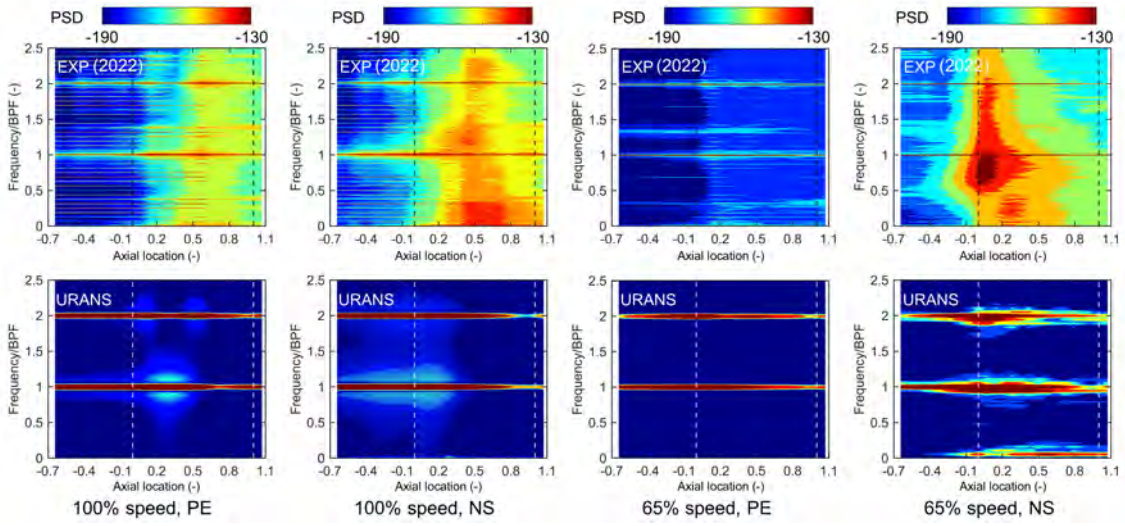

Figure 9: Comparison of power spectrum density contours of the normalized static pressure at the rotor casing.

Figure 10 displays the power spectral density (PSD) spectrum on a logarithmic scale at the axial location of $x/C_{ax} = 21\%$, where the local standard deviation of static pressure is large. The plot also includes the $-7/3$ slope line representing the inertial subrange. The results consistently demonstrate that URANS accurately predicts the blade passing frequency (BPF) and its harmonics, but it underestimates the PSD at frequencies below the BPF (with the exception of the 65% speed, NS condition where a numerical rotating instability signal near 0.1 BPF is captured). The rotor passing frequency is not captured in the URANS simulations, which

is expected due to the periodicity assumption adopted in the simulations. These findings clearly highlight the limitations of URANS, and a satisfactory validation based solely on standard deviation (as presented in Figure 8) does not guarantee that URANS accurately captures the underlying flow physics.

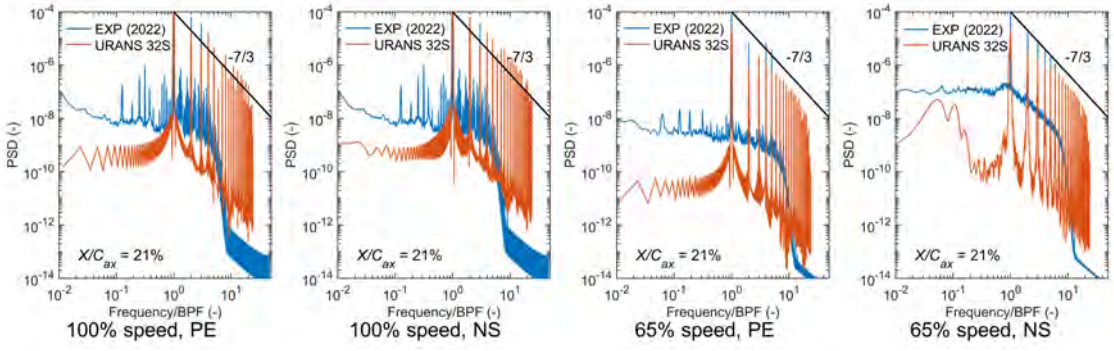

Figure 10: Comparison of power spectrum density curves of the normalized static pressure at the rotor casing.

Although the current URANS study did not capture the sub-BPF flow phenomenon, it is worth noting that previous research did achieve certain success in utilizing URANS to predict the sub-BPF phenomenon [3]. Further review of previous research [2] suggests that a case with a large tip clearance, a fine grid and a small time step are necessary for the accurate prediction of unsteady fluctuations at the sub-BPF scales. Therefore, a grid and time step independence study will be performed on the current compressor for future work. In addition, other factors such as simulating multiple rotor blade passages and running hybrid RANS/LES simulations will also be pursued in the future.

5 ANALYSIS OF UNSTEADY PHENOMENON IN STATOR

This section examines the unsteady phenomena occurring in the stator. Figure 11 displays the PSD results of the static pressure signals that are collected using numerical probes. In addition to the BPF, low frequencies (ranging from 0.05-0.2 times the BPF) are captured by the near-hub probes SP2 and SP3 under various rotational speeds and conditions. The subsequent section will confirm that these low frequencies are produced within the cavity, and thus will not be discussed for now.

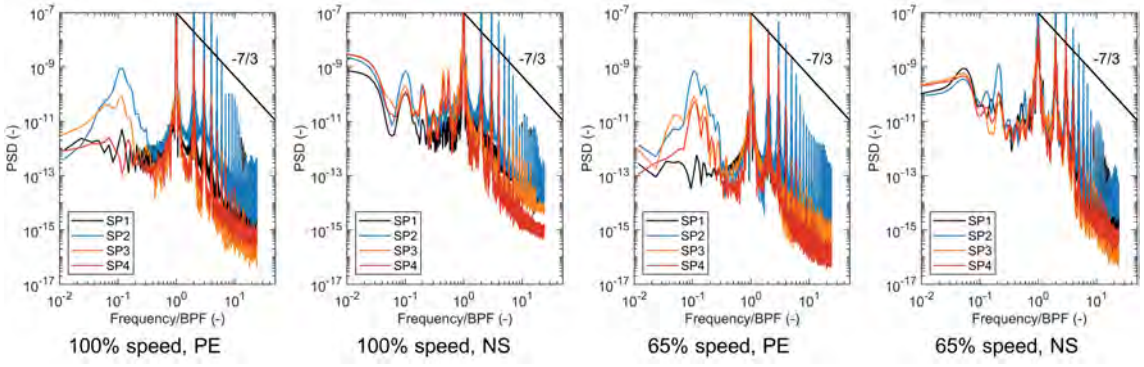

Figure 11: Power spectrum density of static pressure signals in the stator.

Figure 12 shows the standard deviation of the normalized axial velocity (σ_{V_X}/U_{mid}, with U_{mid} denotes the rotor blade speed at midspan) in the vicinity of the stator hub, which helps identify the region with high unsteadiness. Overall, the regions with high unsteadiness are identified at the interface between the mainstream and the corner separation, which reflects the unsteady fluctuation of the corner separation size. In addition, the unsteady fluctuation is stronger at the NS condition than the PE condition, the former of which has a larger time-averaged separation size than the latter.

Combining the observations from Figure 11 and Figure 12, the major unsteadiness in the stator passage originates from the rotor wake at the BPF and its harmonics, which is highly interactive with the stator hub corner separation. To visualize this unsteady phenomenon, Figure 13 presents four snapshots (0T, 0.25T, 0.5T and 0.75T with T denoting the rotor blade passing period T=1/BPF) of the static entropy contours superimposed with the perturbation velocity vector ($V'(t) = V(t) - \bar{V}$) at the 10% span. In these figures, the static entropy can capture the location of the rotor wake and corner separation featuring high entropy loss; the perturbation velocity vector can capture the negative jet phenomenon [25], which refers to the retrograde migration (from the suction side downstream to the pressure side upstream) of the instantaneous wake fluid along the wake trajectory. Since this unsteady flow phenomenon is similar for all four investigated conditions, only results from the PE condition of 100% speed are shown here.

At time instant 0T, the rotor wake, labeled as W1, is located at the LE of the bottom blade. By time instant 0.25T, the rotor wake W1 propagates further downstream and directly impacts the blade suction surface, although it has not yet reached the separation

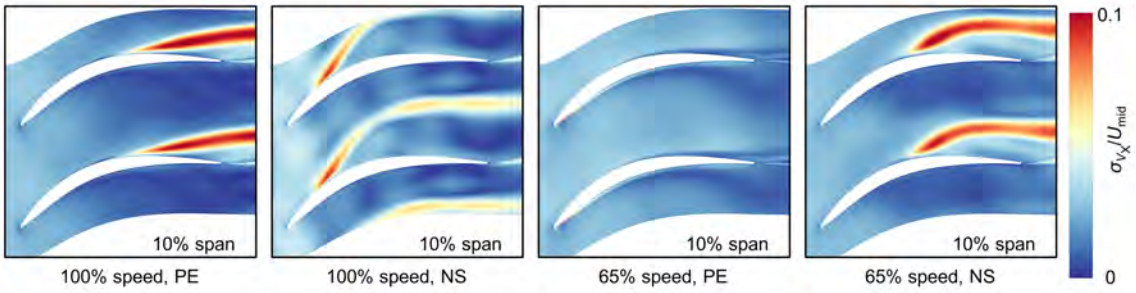

Figure 12: Axial velocity standard deviation in the vicinity of the stator hub.

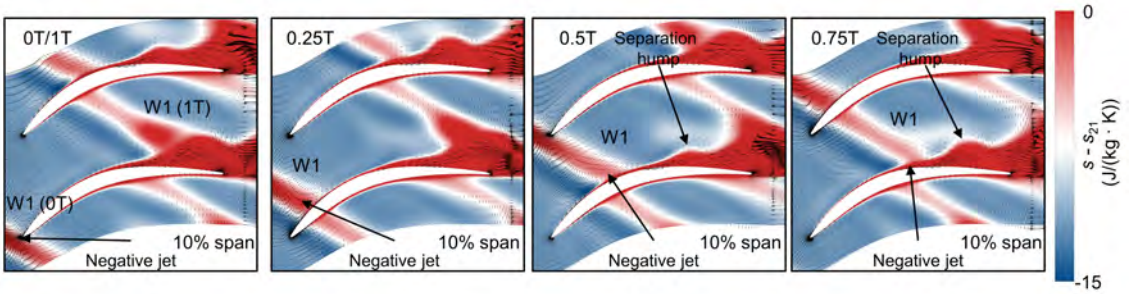

Figure 13: Transient static entropy and perturbation velocity vector of the stator at the PE condition of 100% speed.

point. As a result, the interaction between the rotor wake W1 and the corner separation is barely noticeable. Moving on to time instant 0.5T, the rotor wake W1 impinges on the suction surface nearby the separation point. The negative jet effect migrates the momentum of the suction surface boundary layer away from the wall, resulting in a boundary layer more susceptible to separation. Consequently, a separation hump is induced by the negative jet, representing an instantaneous increase in the corner separation size. At instant 0.75T, the rotor wake W1 traverses through the separation point, resulting in a larger corner separation hump. Finally, at time instant 1T, the rotor wake W1 from the previous rotor period merges with the corner separation, meanwhile the rotor wake W1 from the current rotor period once again reaches the LE of the bottom blade.

6 ANALYSIS OF UNSTEADY PHENOMENON IN CAVITY

In this section, the unsteady phenomena that occur within the cavity are analyzed in detail. Figure 14 presents the PSD results of the static pressure signals within the cavity. These PSD results show similarities with those of the stator, primarily featuring BPF and some low frequencies between 0.05-0.2 times the BPF. It is noteworthy that the highest PSD value of these low frequencies is located at CP3, indicating these low-frequency fluctuations originate near CP3 and propagate along the flow direction.

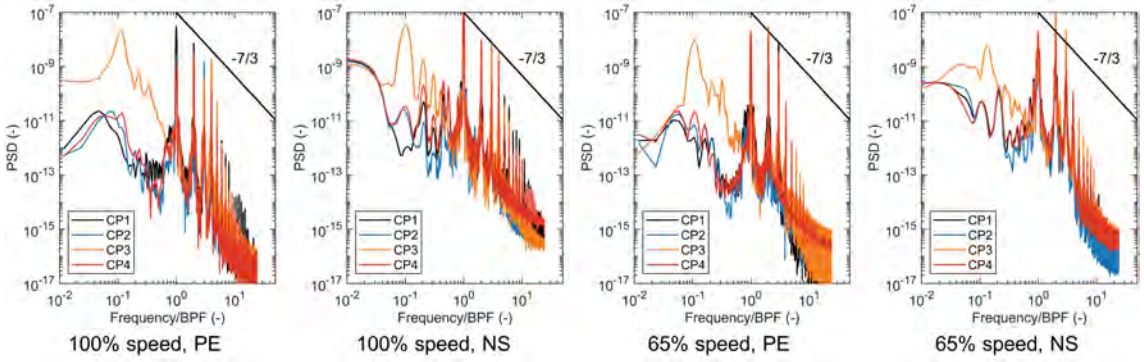

Figure 14: Power spectrum density of static pressure signals in the cavity.

To gain insight into the underlying mechanisms of these low frequencies, Figure 15(a) illustrates the standard deviation of the normalized velocity magnitude at the periodic boundary of the cavity. It is confirmed that the velocity standard deviation in the vicinity of CP3 is significantly higher than the other regions, highlighting its significance in the generation of low frequencies. Since the observations for all the operating conditions are consistent with each other, only the PE condition at the 100% speed is presented for brevity.

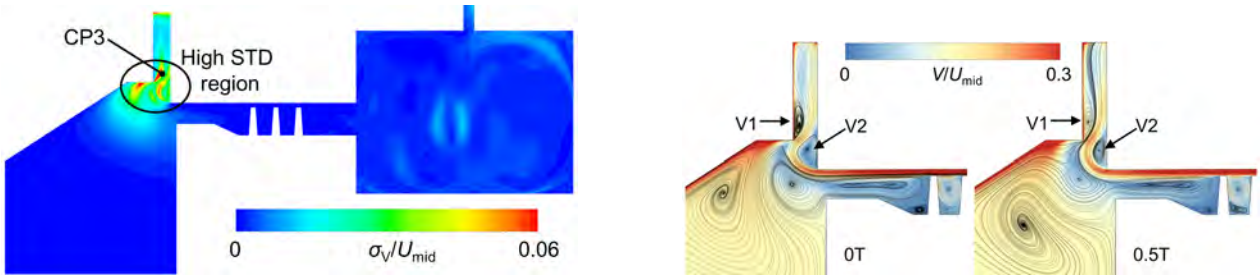

(a) Velocity magnitude standard deviation contours.

(b) Transient velocity magnitude contours and streamline.

Figure 15: Flow field at the cavity periodic boundary, PE condition of 100% speed.

Figure 15(b) illustrates two snapshots of the velocity magnitude contours and the streamlines at the cavity periodic boundary. These snapshots correspond to time instants of 0T and 0.5T, with T denoting the period of the peak signal (i.e., T=1/(0.1 BPF)). Results show that the seal jet flow is suctioned radially outward through the cavity exit, and two vortices are formed between the jet trajectory and the rotor disk (labeled as V1) and between the jet trajectory and the stator disk (labeled as V2). At different time instants, the vortices V1 and V2 shrink and expand periodically, exhibiting a pumping mode. The pumping mode of the vortices can be attributed to the Kelvin-Helmholtz instability of the shear layers between the seal jet and the seal wake. It leads to the unsteady fluctuation of the cavity channel blockage and the cavity leakage flow rates, which affects the main flow of the stator passage as observed previously in Figure 11. However, such an unsteady fluctuation is remarkably small, as the min-max variation of the leakage flow ratio is only about 1% of the time-averaged leakage flow rate at the 100% speed, PE condition of the current case.

7 CONCLUSIONS

In this paper, URANS simulations have been performed to analyze the unsteady flow phenomenon in the TUDa-GLR-OpenStage compressor at stable operating conditions of 100% (transonic) and 65% (subsonic) speeds. The underlying flow mechanisms of each unsteady flow phenomenon were discussed. The main conclusions are drawn as follows:

1. The measured data in the rotor tip region suggests that the unsteadiness of the casing wall pressure is primarily composed of the blade passing signals at the PE condition for both speeds. In contrast, at the NS conditions for both speeds, broadband sub-BPF (about 0.2 BPF at 100% speed and 0.8 BPF at 65% speed) signals associated with the tip leakage flow arise, leading to an increased level of pressure standard deviation. Although URANS results capture the trend of pressure standard deviation well, frequency-domain analysis suggests that it only resolves the blade passing signals and fails to capture any sub-BPF signals associated with the tip leakage flow. For future work, the sensitivity of the URANS method to the choice of grid, time step, and number of passages in the flow domain will be checked.
2. The URANS data in the stator hub region shows that there are two major sources of unsteadiness: the rotor wake impingement at BPF and its harmonics, and the unsteady fluctuation of the cavity leakage at about 0.1 BPF. The intensity of the former unsteadiness is most evident in the stator passage and thus has been analyzed in detail. Flow field analysis reveals that the rotor wake induces a negative jet effect that interacts with the stator suction boundary layer, leading to unsteady fluctuations of the corner separation size and thus the compressor performance.
3. The URANS data in the stator hub cavity indicates the occurrence of a broadband low-frequency (about 0.1 BPF) unsteady flow phenomenon near the cavity exit channel at all investigated operating conditions. Further flow field visualization reveals that this unsteady flow phenomenon corresponds to the pumping mode of the blockage cells in the front cavity well, which is associated with the Kelvin-Helmholtz instability of the seal jet shear layer. The pumping mode leads to an unsteady fluctuation of the blockage size and thus the leakage flow rate. However, the fluctuation of the leakage flow rate is only about 1%, which has a negligible effect on the compressor performance.

ACKNOWLEDGMENT

Hefang Deng, Mingmin Zhu and Jinfang Teng acknowledge the support from the Natural Science Foundation of China (No. 51906140), the Shanghai Municipal Education Commission No. 2023-02-4, the Fundamental Research Funds for the Central Universities, and the United Innovation Center (UIC) of Aerothermal Technologies for Turbomachinery. The TUDa-GLR-OpenStage measurement campaign is supported by the EU-H2020 funded ARiAS project (No. 769346).

DATA AVAILABILITY STATEMENT

The data that support the findings of this study are available from the corresponding author upon reasonable request.

NOMENCLATURE

p	Static pressure
p_t	Total pressure
U	Absolute velocity
η	Adiabatic efficiency
π	Total Pressure ratio

Acronyms

BPF	Blade passing frequency
EXP	Experiment
LE	Leading edge
NS	Near stall
PE	Peak efficiency
PS	Pressure side
PSD	Power spectrum density
SS	Suction side
TE	Trailing edge

REFERENCES

[1] Riera, W., Marty, J., Castillon, L., and Deck, S., 2016. "Zonal Detached-Eddy Simulation Applied to the Tip-Clearance Flow in an Axial Compressor". *AIAA Journal,* ***54***(8), pp. 2377–2391.

[2] Liu, Y., Zhong, L., and Lu, L., 2019. "Comparison of DDES and URANS for Unsteady Tip Leakage Flow in an Axial Compressor Rotor". *Journal of Fluids Engineering,* ***141***(12), p. 121405.

[3] Wang, H., Wu, Y., Wang, Y., and Deng, S., 2020. "Evolution of the Flow Instabilities in an Axial Compressor Rotor with Large Tip Clearance: An Experimental and URANS Study". *Aerospace Science and Technology,* ***96***, p. 105557.

[4] Chen, X., Koppe, B., Lange, M., Chu, W., and Mailach, R., 2022. "Comparison of Turbulence Modeling for a Compressor Rotor at Different Tip Clearances". *AIAA Journal,* ***60***(2), pp. 1186–1198.

[5] Mailach, R., Lehmann, I., and Vogeler, K., 2001. "Rotating Instabilities in an Axial Compressor Originating From the Fluctuating Blade Tip Vortex ". *Journal of Turbomachinery,* ***123***(3), pp. 453–460.

[6] Marz, J., Hah, C., and Neise, W., 2002. "An Experimental and Numerical Investigation into the Mechanisms of Rotating Instability ". *Journal of Turbomachinery,* ***124***(3), pp. 367–374.

[7] Du, J., Lin, F., Zhang, H., and Chen, J., 2010. "Numerical Investigation on the Self-Induced Unsteadiness in Tip Leakage Flow for a Transonic Fan Rotor". *Journal of Turbomachinery,* ***132***(2), p. 021017.

[8] Zhu, M., Teng, J., and Qiang, X., 2021. "Unsteady Near-Stall Flow Mechanisms in a Transonic Compressor Rotor at Different Rotating Speeds". *Aerospace Science and Technology,* ***119***, p. 107124.

[9] Mailach, R., Lehmann, I., and Vogeler, K., 2008. "Periodical Unsteady Flow Within a Rotor Blade Row of an Axial Compressor—Part II: Wake-Tip Clearance Vortex Interaction". *Journal of Turbomachinery,* ***130***(4), p. 041005.

[10] Montomoli, F., Naylor, H. P., and Lapworth, L., 2013. "Unsteady Effects in Axial Compressors: A Multistage Simulation". *Journal of Propulsion and Power,* ***29***(5), pp. 1001–1008.

[11] Saito, S., Yamada, K., Furukawa, M., Watanabe, K., Matsuoka, A., and Niwa, N., 2018. "Flow Structure and Unsteady Behavior of Hub-Corner Separation in a Stator Cascade of a Multi-Stage Transonic Axial Compressor". ASME Paper No. GT2018-76480.

[12] Schulz, H. D., Gallus, H. E., and Lakshminarayana, B., 1990. "Three-Dimensional Separated Flow Field in the Endwall Region of an Annular Compressor Cascade in the Presence of Rotor-Stator Interaction: Part 2—Unsteady Flow and Pressure Field". *Journal of Turbomachinery,* ***112***(4), pp. 679–688.

[13] Ma, W., Ottavy, X., Lu, L., and Leboeuf, F., 2013. "Intermittent Corner Separation in a Linear Compressor Cascade". *Experiments in Fluids,* ***54***, p. 1546.

[14] Liu, Y., Yan, H., Lu, L., and Li, Q., 2017. "Investigation of Vortical Structures and Turbulence Characteristics in Corner Separation in a Linear Compressor Cascade Using DDES". *Journal of Fluids Engineering,* ***139***(2), p. 021107.

[15] Dawkins, I., Taylor, J., Ottavy, X., and Miller, R., 2022. "The Unsteady Topology of Corner Separations". *Journal of Turbomachinery,* ***144***(11), p. 111001.

[16] Wellborn, S. R., 2001. "Details of Axial-Compressor Shrouded Stator Cavity Flows". ASME paper No. GT2001-0495.

[17] Lee, J., Lim, S., Shin, H.-W., Lee, S., and Song, S. J., 2022. "Periodic Unsteady Kinematics of Hub Flows in a Shrouded Multistage Compressor". *Journal of Engineering for Gas Turbines and Power,* ***144***(4), p. 041011.

[18] Klausmann, F., Franke, D., Foret, J., and Schiffer, H.-P., 2022. "Transonic Compressor Darmstadt - Open Test Case Introduction of the TUDa Open Test Case". *Journal of the Global Power and Propulsion Society,* ***6***, pp. 318–329.

[19] Klausmann, F., Franke, D., and Schiffer, H.-P., 2022. "Transonic Compressor Darmstadt Open Test Case – Unsteady Aerodynamics and Stall Inception". Proceedings of Global Power and Propulsion Society. GPPS Paper No. TC2022-0071.

[20] Klausmann, F., Kilian, N., He, X., Franke, D., Schmidt, B., and Schiffer, H.-P., 2023. "Transonic Compressor Darmstadt Open Test Case: Experimental Investigation Of Stator Secondary Flows And Hub Leakage". Turbo Expo: Power for Land, Sea, and Air. ASME Paper No. 2023-103502.

[21] Wallin, S., and Johansson, A. V., 2000. "An Explicit Algebraic Reynolds Stress Model for Incompressible and Compressible Turbulent Flows". *Journal of Fluid Mechanics,* ***403***, p. 89–132.

[22] ANSYS, 2021. "Ansys CFX-Solver Theory Guide, Release 20.1". *ANSYS Help DOC*.

[23] He, X., Zhu, M., Xia, K., Klausmann, F., Teng, J., and Vahdati, M., 2023. "Validation And Verification of RANS Solvers for TUDa-GLR-OpenStage Transonic Axial Compressor". *Journal of the Global Power and Propulsion Society,* ***7***, pp. 13–29.

[24] Welch, P., 1967. "The use of fast fourier transform for the estimation of power spectra: A method based on time averaging over short, modified periodograms". *IEEE Transactions on Audio and Electroacoustics,* ***15***(2), pp. 70–73.

[25] Mailach, R., Lehmann, I., and Vogeler, K., 2008. "Periodical Unsteady Flow Within a Rotor Blade Row of an Axial Compressor—Part I: Flow Field at Midspan". *Journal of Turbomachinery,* ***130***(4), p. 041004.